AMERICAN
METEOROLOGICAL
SOCIETY

Journal of the Atmospheric Sciences

The DOI for this manuscript is doi: 10.1175/JAS-D-18-0174.1

The final published version of this manuscript will replace the preliminary version at the above DOI once it is available.

If you would like to cite this EOR in a separate work, please use the following full citation:

Lee, H., A. Fridlind, and A. Ackerman, 2018: An evaluation of size-resolved cloud microphysics scheme numerics for use with radar observations Part I: Collision-coalescence. J. Atmos. Sci. doi:10.1175/JAS-D-18-0174.1, in press.

An evaluation of size-resolved cloud microphysics scheme numerics for use with radar observations

Part I: Collision-coalescence

Hyunho Lee[1,2], Ann M. Fridlind[2], and Andrew S. Ackerman[2]

[1] Center for Climate Systems Research, Columbia University, New York, NY 10025, U.S.A.

[2] NASA Goddard Institute for Space Studies, New York, NY 10025, U.S.A.

Journal of the Atmospheric Sciences

Submitted June 2018

Revised September 2018

Corresponding author: Hyunho Lee, Center for Climate Systems Research, Columbia University, and NASA Goddard Institute for Space Studies, New York, NY 10025, U.S.A.

E-mail address: hyunho.lee@nasa.gov

Abstract

This study evaluates some available schemes designed to solve the stochastic collection equation (SCE) for collision-coalescence of hydrometeors using a size-resolved (bin) microphysics approach, and documents their numerical properties within the framework of a box model. Comparing three widely used SCE schemes, we find that all converge to almost identical solutions at sufficiently fine mass grids. However, one scheme converges far slower than the other two and shows pronounced numerical diffusion at the large-drop tail of the size distribution. One of the remaining two schemes is recommended on the basis that it is well-converged on a relatively coarse mass grid, stable for large time steps, strictly mass-conservative, and computationally efficient. To examine the effects of SCE scheme choice on simulating clouds and precipitation, two of the three schemes are compared in large-eddy simulations of a drizzling stratocumulus field. A forward simulator that produces Doppler spectra from the large-eddy simulation results is used to compare the model output directly with radar observations. The scheme with pronounced numerical diffusion predicts excessively large mean Doppler velocities and overly broad and negatively skewed spectra compared with observations, consistent with numerical diffusion demonstrated in the box model. Statistics obtained using the recommended scheme are closer to observations, but notable differences remain, indicating that factors other than SCE scheme accuracy are limiting simulation fidelity.

1. Introduction

Modeling of clouds and precipitation has made remarkable advances over the last several decades. Today many microphysical processes occurring in clouds can be evaluated over a wide range of spatial and temporal scales. However, in spite of these advances, the representation of cloud processes in models still suffers from large uncertainties, which limits accurate weather forecasting and climate prediction. For instance, interactions of aerosol and clouds are relatively poorly reproduced in climate models, contributing to large uncertainties in aerosol impacts on climate (e.g., IPCC 2013). Also, the dominant mechanisms of drizzle formation associated with droplet spectral broadening are still debated (e.g., Laird et al. 2000; McGraw and Liu 2004; Wood 2005; Magaritz et al. 2009).

A size-resolved or "bin" cloud microphysics scheme, which divides cloud particles spanning a vast range of sizes commonly into a few tens of bins and evaluates microphysical processes associated with the particles in each size bin, has the great advantage of being capable of realistically simulating the detailed evolution of size distributions of particles in clouds (e.g., Khain et al. 2015 and references therein). However, bin microphysics schemes face the problem of so-called numerical diffusion, which refers to artificial broadening of particle size distributions owing to imprecise numerical solutions (e.g., Cooper et al. 1997; Khain et al. 2000). This phenomenon occurs when particles with arbitrary masses are assigned on a fixed mass grid, and hence it occurs whenever a microphysical process is computed using a bin scheme. Furthermore, errors resulting from the numerical diffusion at the large-particle tail of size distributions become more prominent as the particle size distributions are weighted by higher moments, so they have the potential to become a relatively bigger problem when simulation results obtained using the bin microphysics scheme are compared to cloud radar observations, which are most directly sensitive to the sixth moment of the particle size distribution in the Rayleigh regime. In general, it is therefore an important challenge for bin schemes to adopt numerics that are sufficiently accurate, particularly to minimize numerical diffusion. There have been many attempts to develop accurate numerics that are suitable for bin microphysics schemes (e.g., Kovetz and Olund 1969; Berry and Reinhardt 1974; Bott 1998; Wang et al. 2007) and assess their accuracy (e.g., Seeßelberg et al. 1996; Grabowski et al. 2011).

Recently, Rémillard et al. (2017) reported a series of numerical experiments that simulate fields of stratocumulus using two different large-eddy simulation (LES) models with independent bin microphysics schemes and compared results with cloud radar observations using a forward simulator, with the limited objective of evaluating drizzle size distribution characteristics, which are difficult to evaluate using in situ observations owing primarily to small sample volumes. Results indicated the occurrence of relatively too many large drops compared to radar observations, perhaps attributable to numerical diffusion in solving the stochastic collection equation (SCE) for collision-coalescence of drops in the models and perhaps made more prominent owing to size distribution evaluation using radar. Motivated by those results, this study aims to evaluate the accuracy of schemes that have been utilized for solving the SCE in bin microphysics schemes and to provide a guide for numerics especially suitable for use with cloud radar observations.

For this, we select three widely used SCE schemes, proposed by Berry and Reinhardt (1974, hereafter BR74), Jacobson et al. (1994, hereafter J94), and Bott (2000, hereafter B00). They are evaluated with a vast range of mass bin widths and model time steps, and based on extensive evaluations, we here present a guide for selecting a SCE scheme that is most suitable for simulating clouds and precipitation. In addition, a method for utilizing cloud radar Doppler spectra observations is suggested to further model evaluation. Note that this study considers only one-moment bin microphysics schemes on a geometric bin grid, exploiting converged solutions as a benchmark. Multi-moment bin microphysics schemes (e.g., Tzivion et al. 1999) are not considered here, as their expressions to solve the SCE profoundly depend on bin grid refinement, becoming progressively more complex as the bin grid becomes finer, unlike the three schemes selected for this study, which use the same expressions regardless of bin grid width.

Some important features of the three SCE schemes are documented in Section 2. Model results obtained using a box model and an LES model are presented in Sections 3 and 4, respectively. A summary and conclusions are given in Section 5.

2. Descriptions of the SCE schemes

In this section, we document characteristics of the three schemes that are designed to solve the SCE, which describes the rate of change of particle number concentration from collision-coalescence:

$$\frac{\partial f(m)}{\partial t} = \frac{1}{2}\int_0^m f(m')K(m', m-m')f(m-m')dm' - \int_0^\infty f(m)K(m,m')f(m')dm', \tag{1}$$

where $f(m)dm$ is the particle number concentration in the mass interval of $[m, m + dm]$ and $K(m_1, m_2)$ is the collection kernel of a particle pair with masses m_1 and m_2. The first and second terms on the RHS of (1) correspond to sources and sinks, respectively. Note that the factor of 1/2 appears only when considering collisions between the same kinds of hydrometeor (e.g., collisions between drops).

a. BR74

Berry and Reinhardt (1974) presented a scheme, in which the SCE is treated in its original integro-differential equation form. Number density in the SCE is transformed into mass density, which is now widely used to solve the SCE in many other schemes. Integrations of source and sink terms are calculated using three- to five-point Lagrangian integration coefficients with a special treatment near the zero integrands. A six-point Lagrangian interpolation formula is employed to evaluate mass density at an arbitrary grid point (i.e., at a mass grid point with non-integer index), which is important to calculate integration of the source term, and logarithmic values instead of the original values are used for interpolation. This scheme is known to be highly accurate, and newly developed schemes are typically validated against this scheme (e.g., Bott 1998, 2000; Wang et al. 2007).

Note that the original scheme provided a Lagrangian interpolation formula that can be applied only when drop mass is doubled at every two grid points [(A15)–(A31) in BR74]. This study generalizes the formula by using the nearest six points for interpolation, suitable for an arbitrary mass grid. Following the original treatment, if the right three points contain zero, only the nearest two points are used for interpolation in order to avoid the Runge phenomenon. Furthermore, while the original scheme regards a mass concentration below an arbitrary small value of 10^{-70} g cm^{-3} as zero, this study sets that threshold to 10^{-30} kg m^{-3} in order to allow the scheme to work with the single precision (4-byte floating-point) format that we use throughout.

One aspect of the BR74 scheme that is worth highlighting is that it violates mass conservation. Wang et al. (2007) showed that total mass is not conserved while solving the SCE with the BR74 scheme and the error increases as the mass grid becomes coarser. This feature could cause severe errors under some conditions. Another weakness of the BR74 scheme is numerical instability. Because it solves the SCE using an explicit forward method, the result of the calculation can yield a negative concentration, which is more likely to occur with a large time step or a large number of mass bins. Moreover, while evaluating the mass density at an arbitrary grid point using an interpolation formula, the scheme might be inaccurate if it encounters somewhat complex (i.e., not smooth) shapes of drop size distributions (cf. Khain et al. 2000). Some of these factors will be discussed further below.

b. J94

Jacobson et al. (1994) presented another scheme that solves the SCE in its integro-differential equation form analogous to the BR74 scheme. However, it resolves some problems known in the BR74 scheme. First, by introducing the concept of bin pair interaction (i.e., calculating collision of drops from a bin pair and redistributing newly formed drops into the regular mass grid) and evaluating source and sink terms carefully, the J94 scheme does not need an interpolation method as in the BR74 scheme and conserves drop mass strictly by its formulation. In addition, the method adopts a semi-implicit method in discretizing the SCE, so the scheme is always stable regardless of time step size and does not require iterative calculations. Moreover, there is no arbitrary constant in the scheme while an arbitrary small value is necessary in the BR74 scheme.

However, because the J94 scheme combines the integral equation form and the bin pair interaction, it must calculate a triple loop to evaluate the source term, which might require large computational resources at very fine mass grids. Also, the scheme adopts an essentially linear approximation in introducing the bin pair interaction, which can contribute to numerical diffusion at the large-drop tail of the size distribution (cf. Bott 1998; Wang et al. 2007).

c. B00

Bott (1998) introduced a scheme that uses a pure bin pair interaction to solve the SCE. The scheme calculates collisions of drops from a bin pair following the basic concept of the SCE and redistributes newly formed drops into two adjacent mass bins rather than evaluating source and sink terms by integration. The calculation is performed successively so that the concentration within each bin is updated every calculation, whereas the concentrations within the whole bins are updated all at once after all tendency calculations are completed in the BR74 scheme. Because the scheme calculates the bin pair interaction, it conserves total drop mass exactly within the range of round-off error. Bott (1998) initially adopted linear or parabolic functions to approximate the mass densities of the two adjacent bins and calculate the amount of concentration that is transported to the larger of the two adjacent bins, but Bott (2000) later used an exponential function for the approximation, which considerably reduces the numerical diffusion without any arbitrary non-physical parameter such as $g_{\min}$ in Bott (1998). Some previous studies have stated that the scheme is quite accurate (e.g., Khain et al. 2000; Grabowski et al. 2011), whereas another has reported that it does not converge even at a very fine mass grid (Wang et al. 2007).

One problem of the exponential function adopted in Bott (2000) is that it cannot be used to approximate values that contain zero. By design, the concentration in the smaller one of the two adjacent mass bins cannot be zero at the redistribution stage, but that in the larger one often can be when treating the formation of the largest drops. If the exponential approximation is strictly applied, drops larger than the largest drops in the initial distribution cannot be formed when drop mass is doubled at every bin and collision of drops with the same mass is not allowed. To avoid this problem, the original B00 scheme introduced an arbitrary small number in taking the exponential approximation for zero mass density. Moreover, it utilizes a weight-averaged collision kernel, which is obtained from the kernels at the corresponding bin pair and the four nearest pairs [Eq. (7) of Bott 1998], thereby allowing collision of drops with the same mass even though their terminal velocities are identical. In this study, such an averaged collision kernel is not used owing to a lack of any explicit justification, and a tiny number (the smallest number that the given variable type can take) is used for the approximation.

3. Box model results

A box model considering only collision of drops is used to evaluate the three SCE schemes described above. In the mass grid adopted in this study, the ratio of drop masses of two adjacent bins is constant, and the bin width parameter s in the following equation is used to control the ratio: $m_{i+1}/m_i = 2^{1/s}$, where m_i is the drop mass of the ith bin. Thus, drop mass is doubled at every s bins, and a higher value of s indicates a finer mass grid. The smallest drop radius in the grid is 1 μm. The number of bins is $40s$. Whereas Prat and Barros (2007) used a mixture of geometric and arithmetic mass grids, at least for this study we found that a mixture has little advantage over a purely geometric grid using the same number of bins because the arithmetic grid requires so many more bins to cover a fixed range of drop masses.

While some studies adopt an idealized collection kernel such as a product kernel or the Golovin kernel to examine performance of SCE schemes, particularly to compare the numerical solution obtained using SCE schemes to the analytic solution, it has been shown that an SCE scheme may show a relatively large error using a realistic hydrodynamic collection kernel even if the scheme works well using an idealized collection kernel, mainly attributable to the nonlinearity of the realistic collection kernel (e.g., Wang et al. 2007; Alfonso et al. 2013). Therefore, this study adopts only a realistic hydrodynamic kernel, which is expressed as

$$K(r_1, r_2) = \pi(r_1 + r_2)^2 |V_t(r_1) - V_t(r_2)| \eta, \tag{2}$$

where r_1 and r_2 are the radii of two colliding drops, V_t is the drop terminal velocity, and η is the collection efficiency, which is the product of the collision efficiency and the coalescence efficiency. The terminal velocity of drops follows Beard (1976). Note that the terminal velocity is used only to calculate the collision kernel, and sedimentation is not considered in the box model. The collision efficiency provided in Hall (1980) with a linear interpolation is used. The coalescence efficiency is assumed to be unity. Turbulence-induced collision enhancement (e.g., Ayala et al. 2008; Pinsky et al. 2008; Wang and Grabowski 2009) is not considered in this study.

A gamma distribution with a fixed shape parameter of 6 is used to express the initial drop size distribution in the box model. The liquid water content is 1 g m^{-3}, and the initial drop number concentration is set to 100 cm^{-3}. The model is integrated for 1 h.

a. Comparison of the converged solutions

In order to evaluate the accuracy of an SCE scheme, first it is necessary to obtain the correct solution for a given initial drop size distribution and collection kernel. Although it is impossible to obtain the analytic solution for the condition considered in this study, it is expected that an approximate solution close enough to the correct solution can be obtained if all the SCE schemes yield an identical converged solution at a sufficiently fine mass grid and small time step. Therefore, to obtain the reference solution, a very fine resolution is applied to the box model. The mass bin width parameter *s* is set to 64 so that the number of bins is 2560. The time step is set to 1 s for the J94 and B00 schemes but 0.1 s for the BR74 scheme because when the time step is 1 s the BR74 scheme is unstable (Fig. 11) whereas the other two are almost converged. Note that the same approach was used in Wang et al. (2007), in which *s* = 16 was used to obtain the reference solution.

Figure 1 shows the time evolution of size distributions of number, mass, and reflectivity of drops obtained using each SCE scheme. The time evolution of drop size distributions shown in the figure is typical and similar to that shown in previous studies (e.g., Berry and Reinhardt 1974; Wang et al. 2007; Lkhamjav et al. 2017). The solutions are almost identical regardless of the SCE scheme used. Moreover, each scheme converges to the obtained solution as the mass grid becomes finer, which will be shown in detail in the next section. Therefore, we conclude that the obtained solution can be regarded as effectively correct. In the rest of this work, the solution depicted in Fig. 1 is used as the reference solution against which relative errors under coarse mass grids or large time steps are evaluated.

Note that Wang et al. (2007) reported that the B00 scheme does not yield a converged solution even on a very fine mass grid (*s* = 32). We can only speculate about possible reasons: 1) we identified two typos in Bott (2000)[1] that have not been addressed in a corrigendum, and 2) it is possible that Wang et al. (2007) did not exploit advances in the Bott scheme because they did not refer to Bott (2000), which uses an exponential flux method, and instead only refer to Bott (1998), which uses a linear flux method. In this study, all examined SCE schemes are accurate at a sufficiently fine resolution and we consider them properly implemented since their converged solutions are also identical.

---

[1] One in Eq. (6) and another in Eq. (7).

b. Sensitivity to bin width

It is shown that all three SCE schemes yield a (converged) reference solution. However, the solution can be obtained only at very fine mass grids that are not generally used in typical three-dimensional bin microphysics models owing to computational expense. Therefore, the accuracy of each SCE scheme using mass grids typically adopted by recent cloud models and its rate of convergence are examined. Two types of errors are measured to estimate accuracy: one is the spectral difference in quantities (number, mass, or reflectivity) between the solution obtained at a relatively coarse mass grid and the reference solution [i.e., $x_i - x_{i0}$, where x_i corresponds to number, mass or reflectivity concentration in the *i*th bin, and the subscript 0 indicates the reference solution], and the other is the spectral ratio of the quantities (i.e., x_i / x_{i0}).

Figures 2 and 3 show errors of the J94 scheme relative to the reference solution when s = 1, 2, 4, and 8. The difference in quantities (Fig. 2) shows that the J94 scheme underestimates the number concentration of small drops ($r \sim 10$ μm) in the early stage of the integration and overestimates it in the later stage. Moreover, the scheme overestimates the radar reflectivity factor of large drops ($r \sim 400$ μm) in the later stage of the integration. In addition, although the J94 scheme strictly conserves total drop mass by its formulation, it yields size distributions of mass in which concentrations of relatively small drops are underestimated and those of relatively large drops are overestimated at the large-drop tail of the distributions. These features reveal that the J94 scheme exhibits distinct numerical diffusion, in which concentrations of relatively large drops are overestimated. As the mass grid becomes finer, the difference is reduced, indicating the convergence of the J94 scheme. However, pronounced numerical diffusion is still observed even at a relatively fine mass grid (s = 4 or 8). It is noted that this numerical diffusion is more clearly shown in higher moments of drop size distribution because it occurs at the large-drop tail of the distribution, such that higher moments of the size distribution such as radar reflectivity factor are more sensitive to SCE scheme numerical diffusion.

The ratio of quantities (Fig. 3) more clearly shows the numerical diffusion at the large-drop tail of the distribution. The underestimations of the quantities in specific radius ranges seen in the difference (Fig. 2) are not significant from the perspective of error ratio. On the other hand, at the right tail of distribution, although the overall magnitudes of the quantities are quite small (Fig. 1), the ratios of the obtained solutions under coarse mass grid to the reference solution reach up to a few orders of magnitudes. As with the difference, the numerical diffusion is more pronounced at higher moments.

Figure 4 shows errors of the BR74 scheme when $s = 1$ and 2. The number concentration of small drops ($r \sim 10$ μm) is slightly overestimated, but the difference almost disappears during the integration. Consistent with the BR74 scheme not conserving mass, the size distribution of mass shows a clear decrease in mass, largely resulting from loss of the largest drops. The differences in quantities of the BR74 scheme are considerably smaller than those of the J94 scheme. When $s = 1$, the overall magnitude of difference is similar to that obtained using the J94 scheme with $s = 4$. Furthermore, the differences obtained using the BR74 scheme with $s = 2$ are much smaller than that obtained using the J94 scheme with $s = 8$. As the parameter s increases further beyond 2, differences further decrease rapidly (not shown), which shows that the BR74 scheme converges much faster than the J94 scheme.

Figure 5 shows errors of the B00 scheme when $s = 1$ and 2. The overall pattern of differences obtained using the B00 scheme is similar to that of the BR74 scheme and has the opposite tendency to that of the J94 scheme. The B00 scheme overestimates the number concentration of small drops in the early stage of the integration but underestimates it in the later stage. It shows characteristics of an anti-diffused distribution under coarse mass grids: an overestimation of relatively small drop concentration and an underestimation of relatively large drop concentration at the large-drop tail are seen in the size distributions of mass, and the radar reflectivity of large drops is underestimated. The overall magnitude of error is similar or slightly larger than that of the BR74 scheme, and the B00 scheme also converges rapidly to the reference solution so that error almost disappears when s is increased beyond 2 (not shown).

The time series of Rayleigh-regime total radar reflectivity factors as a function of the bin width parameter s and their deviations from the reference solution are shown in Fig. 6. The BR74 and B00 schemes slightly underestimate the total reflectivity factor under coarse mass grids whereas the J94 scheme considerably overestimates it, consistent with Figs. 2–5. When the BR74 scheme is used, the deviation increases and then tends to converge to a certain level during integration. The BR74 scheme exhibits a very high accuracy and a fast convergence: the maximum error is 4 dBZ when $s = 1$ but is less than 1 dBZ when $s \geq 2$. By contrast, the J94 and B00 schemes exhibit deviations that increase and then decrease after reaching maximum values where the rapid growth of small drops to large drops occurs (Fig. 1). The diffusive characteristic of the J94 scheme is clearly seen in Figs. 6b and 6e. The maximum deviation reaches 17 dBZ at $t = 13$ min when $s = 1$. The deviations decrease by roughly half for each doubling of s in the range from 1 to 8, reaching a maximum of 2 dBZ when $s = 8$. The B00 scheme exhibits a better accuracy than the J94 scheme but a worse accuracy than the BR74 scheme. While it also shows negative deviations as in the BR74 scheme, the maximum deviation reaches only 6 dBZ when $s = 1$. Its rate of convergence is faster than that of the J94 scheme and the deviations decrease by roughly two thirds for each doubling of s in the range from 1 to 8.

c. Sensitivity to time step size

In addition to convergence with mass grid refinement, convergence of the SCE schemes with decreasing time step is also examined. In the previous section, it is shown that higher moments of the size distribution exhibit more pronounced errors. We therefore examine total radar reflectivity factor to investigate convergence here. Figure 7 shows the time series of deviation of total radar reflectivity factor. The bin width parameter *s* is fixed at 2. The time step is reduced from 10 s to 2 s, and 1 s is used as the reference time step for the J94 and B00 schemes and 0.1 s for the BR74 scheme.

The maximum deviations for all schemes occur between 10–20 min, when the rapid growth of small drops to large drops occurs, as seen in Figs. 6e and 6f. The BR74 scheme develops predominantly negative deviations, whereas the deviations for J94 and B00 schemes are always positive. The BR74 scheme develops by far the greatest error among the considered schemes. When the time step is 10 s, the maximum deviation in the BR74 scheme is up to 4 dBZ, but the maximum deviations are less than 1 dBZ both in the J94 and B00 schemes. In particular, the deviations for the B00 scheme are extremely small for the considered time step lengths.

Figure 8 summarizes the previous results by showing the maximum deviations in the total radar reflectivity factor with respect to the bin width parameter *s* and time step Δt. The deviations resulting from coarse mass grids and large time steps are both negative in the BR74 scheme, positive in the J94 scheme, and have opposite signs in the B00 scheme. The sense of these deviations implies that in a typical (i.e., computationally feasible) model configuration, formation of large particles will likely be delayed in the BR74 scheme versus accelerated in the J94 scheme, and the deviations will tend to offset each other in the B00 scheme. For example, when the time step is 5 s and the bin width parameter *s* is 2, which is a typical LES configuration as well as the configuration used in our LES study described in the next section, the maximum deviations of the BR74, J94, and B00 schemes to the reference solution are –2.3 dBZ, 9.7 dBZ, and –2.2 dBZ, respectively.

d. Computational efficiency

Figure 9 shows the computational time required to solve the SCE for 1 h with a time step of 1 s as a function of the bin width parameter *s* proportional to the number of bins. The BR74 scheme is fastest, followed by the B00 and the J94 schemes. Note that some previous studies pointed out that the BR74 scheme is computationally inefficient (e.g., Bott 1998; Khain et al. 2000), presumably attributable to the slow convergence rate of the BR74 scheme with respect to time step (Fig. 7). It is seen that the BR74 and B00 schemes scale as ~$O(n^2)$, where n is the number of bins, whereas the J94 scheme scales as ~$O(n^3)$. While both solving the integro-differential SCE equation over all bins and calculating all bin pair interactions have a complexity of $O(n^2)$, the J94 scheme scales as $O(n^3)$ by virtue of the combination of visiting all bins, which has a complexity of $O(n)$, and evaluating all possible bin pair interactions at each bin, which has a complexity of $O(n^2)$.

It should be noted that actual computational times will vary depending on optimization techniques, and hence it is difficult to determine which of the schemes is the fastest under a specific model setup. Instead, it can be only concluded that the J94 scheme would be much slower than the other schemes as the number of bins increases because of its high complexity.

e. Numerical stability and mass conservation of the BR74 scheme

In addition to the rate of convergence, conservation of total mass is a highly desirable requirement since otherwise ad hoc corrections are required to force conservation. Besides accuracy, numerical stability of a scheme (e.g., Courant–Friedrichs–Lewy condition) also merits examination. It is known that the BR74 scheme does not conserve mass nor is it numerically stable (Bott 1998; Khain et al. 2000).

The numerical stability of the BR74 scheme is examined by a 1-h integration with varying time steps and bin width parameters. If the total mass diverges during the integration, it is determined that the BR74 scheme is unstable under that condition. It is noted that such instability always developed within 10 min of integration in all cases for the given initial drop size distribution and collision kernel. Figure 10 shows the criteria for stability of the BR74 scheme. When $s \leq 4$, the BR74 scheme is always stable when the time step is less than or equal to 20 s. When $s = 8$, the BR74 scheme requires a model time step shorter than 10 s, and the required time step becomes shorter as the mass grid becomes finer. Roughly, the largest allowed time step halves as the logarithm of bin grid width halves. It is noted that unconditional stability is important in principle, but the instability of the BR74 scheme may not be a common problem when considering conditions used in typical numerical simulations.

Figure 11 shows the time series of total drop mass in the BR74 scheme. Because the box model allows only collision of drops, total drop mass should be constant during the integration. However, mass loss is evident in the experiments using the BR74 scheme. It is shown that mass grid spacing has much more impact on the error than time step size. The error tends to increase with time except at the early stage of integration, and it reaches up to ~40% at $t = 1$ h using the coarsest mass grid. Khain et al. (2000) also reported that the BR74 scheme can cause ~30% mass loss under specific conditions. Wang et al. (2007) showed that the error in total mass of the BR74 scheme is a few percent at a specific instance (when large drops start to form in their study), and its magnitude is also comparable to that found here (at $t \sim 10$–20 min in this study).

4. 3-D LES model results

a. Model description and experimental setup

In the previous section, it is found that in the simplistic framework of a box model, the evolution of drop size distribution can vary depending on accuracy of the SCE scheme. To examine the effects of SCE scheme on cloud development and drizzle formation in a more realistic framework, the J94 and B00 schemes are implemented in an LES model and drizzling stratocumulus is simulated. The Distributed Hydrodynamic Aerosol and Radiative Modeling Application (DHARMA) model (Ackerman et al. 2004 and references therein) is used as the LES model here. The DHARMA model adopts the Community Aerosol-Radiation-Microphysics Application (CARMA) (Ackerman et al. 1995; Jensen et al. 1998) size-resolved bin microphysics model to treat drop nucleation, condensation, evaporation, sedimentation, and collision-coalescence. With the notable exception of the collision-coalescence scheme, the microphysics model is identical to that used in Rémillard et al. (2017).

To evaluate model results, the W-band Atmospheric Radiation Measurement (ARM) cloud radar (WACR; Mead and Widener 2005) Doppler spectra observations are used. To directly compare model results with the radar observations, the McGill Radar Doppler Spectra Simulator (MRDSS; Kollias et al. 2014), a forward radar simulator that produces radar observation products from bin microphysics scheme outputs and information about turbulence, is applied.

Following Rémillard et al. (2017), we simulate a case study of drizzling stratocumulus observed on 22 Nov 2009 during the Clouds, Aerosols, and Precipitation in the Marine Boundary Layer (CAP-MBL) campaign (Wood et al. 2015). The environment is characterized by a relatively well-mixed boundary layer topped by a strong inversion at z ~ 1.6 km. The initial profiles of potential temperature, water vapor mixing ratio, and horizontal wind speed are shown in Rémillard et al. (2017).

For the collision efficiency, a parameterization suggested by Böhm (1999) is used; results are not sensitive to alternatively adopting the Hall (1980) kernel (not shown). Coalescence efficiency between drops is assumed to be unity; results are not sensitive to alternatively using Beard and Ochs (1984) coalescence efficiencies (not shown). To promote drizzle formation, a relatively low aerosol concentration of 65 cm^{-3} with a bimodal log-normal distribution, in which modes at radii of 20 and 50 nm, geometric standard deviations of 1.1 and 1.4, and number concentrations of 19 and 46 cm^{-3}, respectively (see also Rémillard et al. 2017), are specified. The aerosol treatment is diagnostic following previous studies (e.g., Clark 1974; Ackerman et al. 2004; Rémillard et al. 2017), in which evaporation of all drops recovers the initial aerosol distribution in a grid cell. The number of mass bins is set to 70 with $s = 2$. An adaptive time step between 4–5 s is used for dynamics and collision-coalescence. The horizontal grid spacing is 75 m, and the vertical grid spacing is varied between ~10–20 m below $z = 1.6$ km with the finest vertical grid spacing at the surface and the top of the boundary layer. The domain size is $4.8 \times 4.8 \times 2.5\ \text{km}^3$. Model integration is performed for 18 h, and the last 6 h is used for the analysis. The simulation using the J94 scheme in this study is the same as a simulation in Rémillard et al. (2017, the DHARMA65b case) except for minor changes in the LES model and forward radar simulator codes that do not substantially impact results, as well as three times longer simulation duration in order to develop drizzle intensity more comparable to observations.

b. Drizzle properties

Figure 12 shows the contoured frequency by altitude diagrams (CFADs) of radar reflectivity factors obtained using the J94 and B00 schemes and from the cloud radar observations of W-band backscattering radar cross sections. Radar reflectivity factor is binned by 2 dBZ intervals. Both the simulations and observations are filtered by a range of liquid water path (LWP) between roughly 120 and 200 g m^{-2} which correspond to one standard deviation below and above the mean LWP in the simulations, respectively. All the simulated and observed CFADs share some important features: 1) the highest reflectivities are located near cloud base, 2) the narrowest distributions are located in the upper cloud layer with a peak probability corresponding to around –15 dBZ, and 3) the contours indicate a tilted structure to the left as the altitude decreases below cloud base, corresponding to a decrease in mean reflectivity with decreasing altitude. Note that the decrease in mean reflectivity with decreasing altitude is attributable to evaporation, but the differences in evaporation below cloud base between the two simulations are negligible (not shown).

Despite those similarities, the CFADs obtained using the J94 scheme and from the observations show some distinct differences. A low reflectivity region (radar reflectivity factor of about –30 to –40 dBZ) just below cloud base is clearly seen in the observations but absent in the simulation. Moreover, the probability distribution as a function of altitude below cloud base is consistently narrower in the simulation than in the observations. The simulated CFAD using the J94 scheme is also less tilted below cloud base than in the observations; for example, the peak at $z \sim 0.6$ km appears at –25 dBZ in the simulation but at –35 dBZ in the observations. We note that using higher aerosol number concentration (up to 260 cm^{-3}) reduces radar reflectivities overall, but does not reduce the tilt and width biases (not shown).

Using the B00 scheme, the relatively low reflectivity region below cloud base that is not reproduced using the J94 scheme is evident. The probability distributions below cloud base are broader than those in the simulation using the J94 scheme, and the centers of the distributions are more tilted toward the lower reflectivity values. Although there remain some discrepancies compared to the observations, which can be affected by many factors other than numerics of collision-coalescence, the CFAD obtained using the B00 scheme is generally closer to the observations than that obtained using the J94 scheme.

To evaluate the results of the bin microphysics model in more detail, moments of Doppler spectra are compared. Figure 13 shows the mean Doppler velocity, spectral width, and skewness as a function of radar reflectivity factor and altitude, with median value plotted at each bin of reflectivity and altitude. The observed mean Doppler velocity shows very small values near cloud top regardless of reflectivity, indicating that the region is mainly occupied by small droplets. The magnitude of mean Doppler velocity (negative downward) generally increases with increasing reflectivity and decreasing height. Such general features are well reproduced in both simulations. In spite of the similar trend, however, the B00 scheme yields consistently smaller magnitude of mean Doppler velocities compared to the J94 scheme, and the decreased mean Doppler velocity magnitude obtained using the B00 scheme is closer to the observations than that using the J94 scheme.

In addition to the mean Doppler velocity distribution, the width of Doppler spectra obtained using the J94 and B00 schemes share some similarities. The width of Doppler spectra below cloud base is seen to generally increase with increasing reflectivity both in the simulations and observations, but the increase in the width of spectra is more pronounced in the observations than in the simulations. In spite of the common discrepancy between the simulated and observed widths of Doppler spectra below cloud base, the magnitude of the width of Doppler spectra obtained using the B00 scheme is consistently smaller than that of the J94 scheme and closer to the observations. Furthermore, when focusing within the cloud layer, the width of Doppler spectra obtained using the B00 scheme is quite similar to the observations but is overestimated using the J94 scheme.

The Doppler spectra using the J94 scheme are too negatively skewed especially near the cloud base and at low radar reflectivities, indicative of a longer tail of fast-falling drops. In contrast, the majority of observed Doppler spectra are positively skewed below cloud base, indicative of a longer tail of slow-falling drops. The skewness using the B00 scheme effectively vanishes below cloud base. The observed skewness within cloud increases from negative to positive with increasing reflectivity except near cloud top, which is roughly reproduced in the simulation using the B00 scheme whereas the J94 scheme shows predominantly negative skewness. In general, the B00 scheme corrects most of the negatively biased skewness obtained using the J94 scheme, improving agreement with observations, but there are still clear deviations; particularly at high radar reflectivities below cloud base.

In addition to the moments of Doppler spectra, drop size distributions from the two simulations are directly compared. Figure 14 shows normalized spectra of drop number concentration and radar reflectivity factor averaged near and below cloud base. The size distributions of drop number concentration become broader with decreasing height in both simulations, and it is clearly seen that the B00 scheme reduces the numerical diffusion at the large-drop tail of distributions. Moreover, the spectra of radar reflectivity factor reveal the characteristics discussed above: slower mean drop fall speed, and narrower, less negatively skewed spectra using B00 relative to the J94 scheme.

Overall, the J94 scheme yields excessive mean Doppler velocity, overly broad spectra, and negatively skewed spectra compared to the observations. It is straightforward to conclude that all these features are closely associated with the strong numerical diffusion at the large-drop tail of drop size distributions for the J94 scheme, which were evident in the box model analysis. The B00 scheme, which more accurately solves the SCE and considerably reduces numerical diffusion compared to the J94 scheme, resolves these shortcomings of the simulated Doppler spectra to a large extent. However, the simulated Doppler spectra using the B00 scheme still show differences compared to the observations. These differences might be attributable to inadequate numerics for other microphysical processes such as activation, vapor diffusional process (condensation and evaporation), sedimentation, or breakup of large drops. Physically more complete descriptions of the microphysical processes, for example, turbulence-induced collision enhancement (Ayala et al. 2008; Pinsky et al. 2008; Wang and Grabowski 2009), or considering multiple collisions within a finite time step (Lkhamjav et al. 2017) might also contribute to resolving the differences between simulations and observations. As briefly discussed by Rémillard et al. (2017), problems related to averaging observed Doppler spectra in a turbulent environment might also lead to some differences. In future work we will first address other sources of error associated with numerics.

5. Summary and Conclusions

In order to provide a guide for modeling collision-coalescence process suitable for a bin cloud microphysics scheme, this study selected three extant schemes for solving the stochastic collection equation (SCE) and evaluated them.

First the schemes were evaluated using a simple box model in which only the collision-coalescence process is considered. The evolution of drop size distributions weighted by number

(0^{th} moment), mass (3^{rd} moment), and Rayleigh-regime reflectivity (6^{th} moment) was examined. All the three schemes yield a solution at very refined mass grids that can be regarded as correct. However, the rates of convergence of the SCE schemes differ significantly. The schemes of Bott (2000; B00) and of Berry and Reinhardt (1974; BR74) exhibit relatively fast convergence rates with respect to mass bin size, yielding solutions close to the correct solution under computationally practical mass grids. However, the scheme documented by Jacobson et al. (1994; J94) converges at a comparatively slow rate and yields pronounced numerical diffusion at the large-drop tail of the size distribution. When considering other properties (convergence rate with respect to the time step, mass conservation, numerical stability, and computational efficiency), the B00 scheme is recommended over the other two. Based on the box model results, we suggest that the B00 scheme with a ratio of masses between the two adjacent bins of less than $\sqrt{2}$ may be adequately accurate for warm cloud simulation. Notably the B00 scheme is not numerically unstable even when the time step is a few tens of seconds, in contrast to the BR74 scheme, which exhibits instability at relatively large time steps or refined mass grids. Note that the numerical schemes considered in this study are all one-moment bin microphysics schemes. An alternative scheme, which takes additional moments into account (e.g., Tzivion et al. 1999), might also be considered. However, such a scheme also seems to require model resolutions (both in bin grid widths and time step) equivalent to those found here required to obtain converged solutions, despite its low flexibility.

The B00 and J94 schemes were then tested in a large-eddy simulation (LES) of stratocumulus observed during the CAP-MBL campaign. Results were compared with W-band cloud radar Doppler spectra, and a forward radar simulator that produces Doppler spectra using the bin microphysics model outputs was utilized for a direct comparison of model results and observations. The highest moment considered, corresponding to reflectivity-weighted drop size distributions, is most sensitive to numerical diffusion of the SCE schemes. The distinct numerical diffusion at the large-drop tail of size distribution evident in the J94 scheme produces Doppler spectra of drizzle with excessive mean velocity and width, and negatively biased skewness (i.e., a longer tail of fast-falling drops) compared to the observations, particularly below cloud base. By reducing numerical diffusion, the B00 scheme corrects those errors to a large extent, but there remain some discrepancies compared with observations, which may be caused by other inadequacies in physical and numerical schemes employed, requiring additional study.

Although the use of cloud radar Doppler spectra is motivated here primarily by the sparsity of in situ measurements to constrain simulated 3-D fields of evolving cloud and drizzle, such spectra may also be useful to constrain simulated warm cloud processes in detail, in the sense that some other observational quantities that have been traditionally used (e.g., liquid water path, cloud fraction, or drop number concentration) may show similar trends regardless of the choice of SCE scheme and resulting drizzle properties (cf. Rémillard et al. 2017). Using such a high moment as radar reflectivity serves as a stringent test of numerics, not only for solution of the SCE but also for other processes, which will be the focus of follow-on work.

Acknowledgments.

This work was supported by the Office of Science (BER), U.S. Department of Energy, under Agreement DE-SC0016237, and by the NASA Radiation Science Program. Resources supporting this work were provided by the NASA High-End Computing (HEC) Program through the NASA Advanced Supercomputing (NAS) Division at Ames Research Center. The original forward radar simulator code was obtained from https://you.stonybrook.edu/radar/research/radar-simulators/software/. Radar observations were obtained from the U.S. Department of Energy

Atmospheric Radiation Measurement (ARM) program (http://www.archive.arm.gov/discovery/). The authors thank J. Rémillard and P. Kollias for providing their forward radar simulator setup and for valuable discussions.

References

Ackerman, A. S., O. B. Toon, and P. V. Hobbs, 1995: A model for particle microphysics, turbulent mixing, and radiative transfer in the stratocumulus-topped marine boundary layer and comparisons with measurements. *J. Atmos. Sci.*, **52**, 1204–1236, https://doi.org/10.1175/1520-0469(1995)052<1204:AMFPMT>2.0.CO;2.

Ackerman, A. S., M. P. Kirkpatrick, D. E. Stevens, and O. B. Toon, 2004: The impact of humidity above stratiform clouds on indirect aerosol climate forcing. *Nature*, **432**, 1014–1017, https://doi.org/10.1038/nature03174.

Alfonso, L., G. B. Raga, and D. Baumgardner, 2013: The validity of the kinetic collection equation revisited – Part 3: Sol–gel transition under turbulent conditions. *Atmos. Chem. Phys.*, **13**, 521–529, https://doi.org/10.5194/acp-13-521-2013.

Ayala, O., B. Rosa and L.-P. Wang, 2008: Effects of turbulence on the geometric collision rate of sedimenting droplets. Part 2. Theory and parameterization. *New J. Phys.*, **10**, 075016, https://doi:10.1088/1367-2630/10/7/075016.

Beard, K. V., 1976: Terminal velocity and shape of cloud and precipitation drops aloft. *J. Atmos. Sci.*, **33**, 851–864, https://doi.org/10.1175/1520-0469(1976)033<0851:TVASOC>2.0.CO;2.

Beard, K. V., and H. T. Ochs III, 1984: Collection and coalescence efficiencies for accretion. *J. Geophys. Res.*, **89**, 7165–7169, https://doi.org/10.1029/JD089iD05p07165.

Berry, E. X., and R. L. Reinhardt, 1974: An analysis of cloud drop growth by collection: Part I. Double distributions. *J. Atmos. Sci.*, **31**, 1814–1824, https://doi.org/10.1175/1520-0469(1974)031<1814:AAOCDG>2.0.CO;2.

Böhm, J. P., 1999: Revision and clarification of "A general hydrodynamic theory for mixed-phase microphysics". *Atmos. Res.*, **52**, 167–176, https://doi.org/10.1016/S0169-8095(99)00033-2.

Bott, A., 1998: A flux method for the numerical solution of the stochastic collection equation. *J. Atmos. Sci.*, **55**, 2284–2293, https://doi.org/10.1175/1520-0469(1998)055<2284:AFMFTN>2.0.CO;2.

Bott, A., 2000: A flux method for the numerical solution of the stochastic collection equation: Extension to two-dimensional particle distributions. *J. Atmos. Sci.*, **57**, 284–294, https://doi.org/10.1175/1520-0469(2000)057<0284:AFMFTN>2.0.CO;2.

Clark, T. L., 1974: A study in cloud phase parameterization using the gamma distribution. *J. Atmos. Sci.*, **31**, 142–155, https://doi.org/10.1175/1520-0469(1974)031,0142:ASICPP.2.0.CO;2.

Cooper, W. A., R. T. Bruintjes, and G. K. Mather, 1997: Calculations pertaining to hygroscopic seeding with flares. *J. Appl. Meteor.*, **36**, 1449–1469, https://doi.org/10.1175/1520-0450(1997)036<1449:CPTHSW>2.0.CO;2.

Grabowski, W. W., M. Andrejczuk, and L.-P. Wang, 2011: Droplet growth in a bin warm-rain scheme with Twomey CCN activation. *Atmos. Res.*, **99**, 290–301, https://doi.org/10.1016/j.atmosres.2010.10.020.

Hall, W. D., 1980: A detailed microphysics model within a two-dimensional dynamic framework: Model description and preliminary results. *J. Atmos. Sci.*, **37**, 2486–2507, https://doi.org/10.1175/1520-0469(1980)037<2486:ADMMWA>2.0.CO;2.

IPCC, 2013: *Climate Change 2013: The Physical Science Basis.* Cambridge University Press, 1552 pp.

Jacobson, M. Z., R. P. Turbo, E. J. Jensen, and O. B. Toon, 1994: Modeling coagulation among particles of different composition and size. *Atmos. Environ.*, **28**, 1327–1338, https://doi.org/10.1016/1352-2310(94)90280-1.

Jensen, E. J., and Coauthors, 1998: Ice nucleation processes in upper tropospheric wave-clouds observed during SUCCESS. *Geophys. Res. Lett.*, **25**, 1363–1366, https://doi.org/10.1029/98GL00299.

Khain, A., M. Ovtchinnikov, M. Pinsky, A. Pokrovsky, and H. Krugliak, 2000: Notes on the state-of-the-art numerical modeling of cloud microphysics. *Atmos. Res.*, **55**, 159–224, https://doi.org/10.1016/S0169-8095(00)00064-8.

Khain, A., and Coauthoers, 2015: Representation of microphysical processes in cloud-resolving models: Spectral (bin) microphysics versus bulk parameterization. *Rev. Geophys.*, **53**, 247–322, https://doi.org/10.1002/2014RG000468.

Kollias, P., S. Tanelli, A. Battaglia, and A. Tatarevic, 2014: Evaluation of EarthCARE cloud profiling radar Doppler velocity measurements in particle sedimentation regimes. *J. Atmos. Oceanic Technol.*, **31**, 366–386, https://doi.org/10.1175/JTECH-D-11-00202.1.

Kovetz, A., and B. Olund, 1969: The effect of coalescence and condensation on rain formation in a cloud of finite vertical extent. *J. Atmos. Sci.*, **26**, 1060–1065, https://doi.org/10.1175/1520-0469(1969)026<1060:TEOCAC>2.0.CO;2.

Laird, N. F., H. T. Ochs III, R. M. Rauber, and L. J. Miller, 2000: Initial precipitation formation in warm Florida cumulus. *J. Atmos. Sci.*, **57**, 3740–3751, https://doi.org/10.1175/1520-0469(2000)057<3740:IPFIWF>2.0.CO;2.

Lkhamjav, J., H. Lee, Y.-L. Jeon, and J.-J. Baik, 2017: Examination of an improved quasi-stochastic model for the collisional growth of drops. *J. Geophy. Res. Atmos.*, **122**, 1713–1724, https://doi.org/10.1002/2016JD025904.

Magaritz, L., M. Pinsky, O. Krasnov, and A. Khain, 2009: Investigation of droplet size distributions and drizzle formation using a new trajectory ensemble model. Part II: Lucky parcels. *J. Atmos. Sci.*, **66**, 781–805, https://doi.org/10.1175/2008JAS2789.1.

McGraw, R., and Y. Liu, 2004: Analytic formulation and parametrization of the kinetic potential theory for drizzle formation. *Phys. Rev. E*, **70**, 031606, https://doi.org/10.1103/PhysRevE.70.031606.

Mead, J. B., and K. B. Widener, 2005: W-band ARM cloud radar. *32nd Int. Conf. on Radar Meteorology*, Albuquerque, NM, Amer. Meteor. Soc., http://ams.confex.com/ams/pdfpap-ers/95978.pdf.

Pinsky, M., A. Khain, and H. Krugliak, 2008: Collisions of cloud droplets in a turbulent flow. Part V: Application of detailed tables of turbulent collision rate enhancement to simulation of droplet spectra evolution. *J. Atmos. Sci.*, **65**, 357–374, https://doi.org/10.1175/2007JAS2358.1.

Prat, O. P., and A. P. Barros, 2007: A robust numerical solution of the stochastic collection-breakup equation for warm rain. *J. Appl. Meteor. Climatol.*, **46**, 1480–1497, https://doi.org/10.1175/JAM2544.1.

Rémillard, J., and Coauthors, 2017: Use of cloud radar Doppler spectra to evaluate stratocumulus drizzle size distributions in large-eddy simulations with size-resolved microphysics. *J. Appl. Meteor. Climatol.*, **56**, 3263–3283, https://doi.org/10.1175/JAMC-D-17-0100.1.

Seeßelberg, M., T. Trautmann, and M. Thorn, 1996: Stochastic simulations as a benchmark for mathematical methods solving the coalescence equation. *Atmos. Res.*, **40**, 33–48, https://doi.org/10.1016/0169-8095(95)00024-0.

Tzivion, S., T. G. Reisin, and Z. Levin, 1999: A numerical solution of the kinetic collection equation using high spectral grid resolution: A proposed reference. *J. Comp. Phys.*, **148**, 527–544.

Wang, L.-P., and W. W. Grabowski, 2009: The role of air turbulence in warm rain initiation. *Atmos. Sci. Lett.*, **10**, 1–8, https://doi.org/10.1002/asl.210.

Wang, L.-P., Y. Xue, and W. W. Grabowski, 2007: A bin integral method for solving the kinetic collection equation. *J. Comp. Phys.*, **226**, 59–88, https://doi.org/10.1016/j.jcp.2007.03.029.

Wood, R., 2005: Drizzle in stratiform boundary layer clouds. Part I: Vertical and horizontal structure. *J. Atmos. Sci.*, **62**, 3011–3033, https://doi.org/10.1175/JAS3529.1.

Wood. R., and Coauthors, 2015: Clouds, aerosols, and precipitation in the marine boundary layer: An ARM mobile facility deployment. *Bull. Amer. Meteor. Soc.*, **96**, 419–440, https://doi.org/10.1175/BAMS-D-13-00180.1.

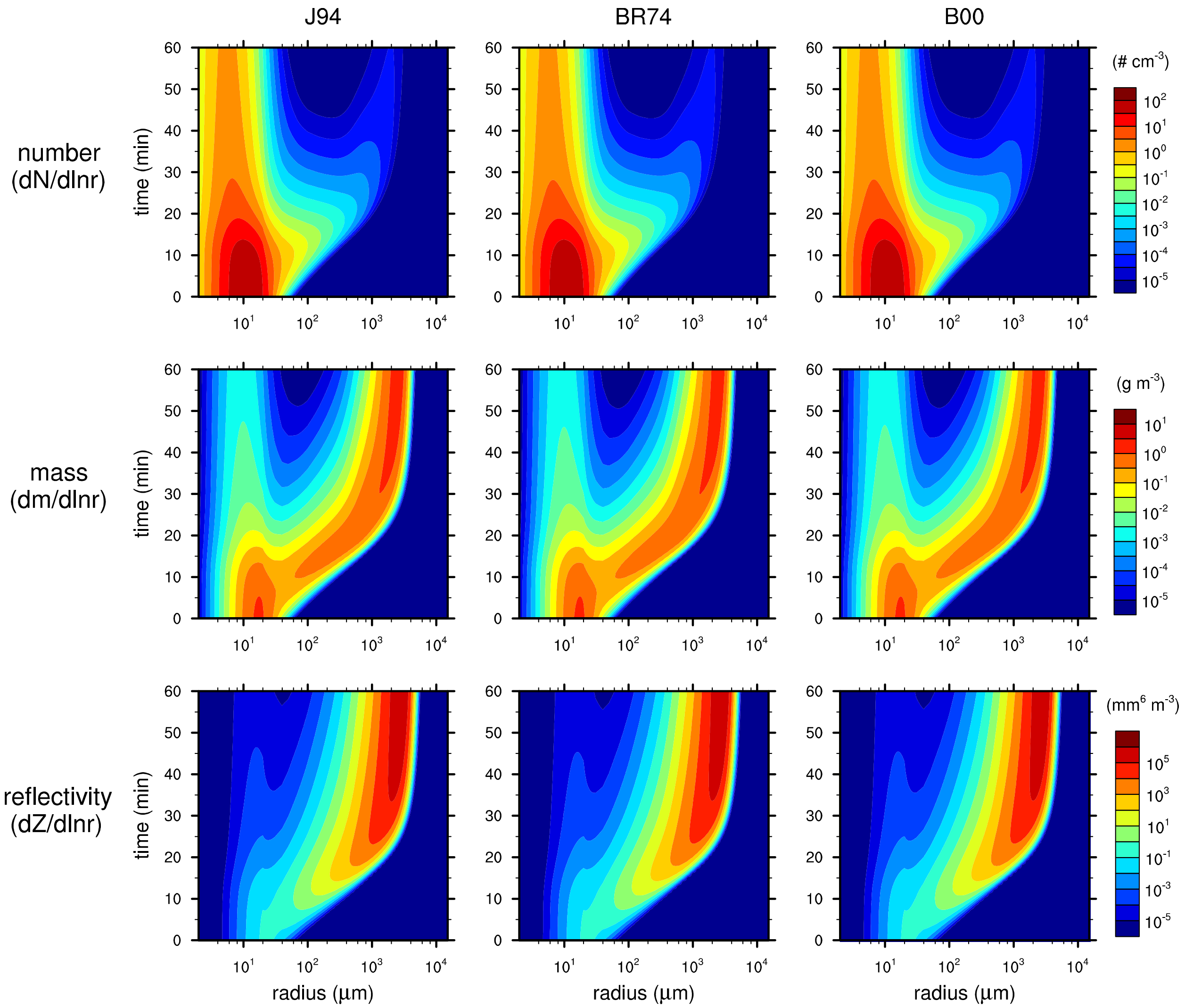

Fig. 1. Time evolutions of size distributions of (top) number, (middle) mass, and (bottom) radar reflectivity factor of drops using the (left) J94, (center) BR74, and (right) B00 schemes. A very fine mass grid and temporal resolution (s = 64, Δt = 1 s for the J94 and the B00 schemes and 0.1 s for the BR74 scheme) is used.

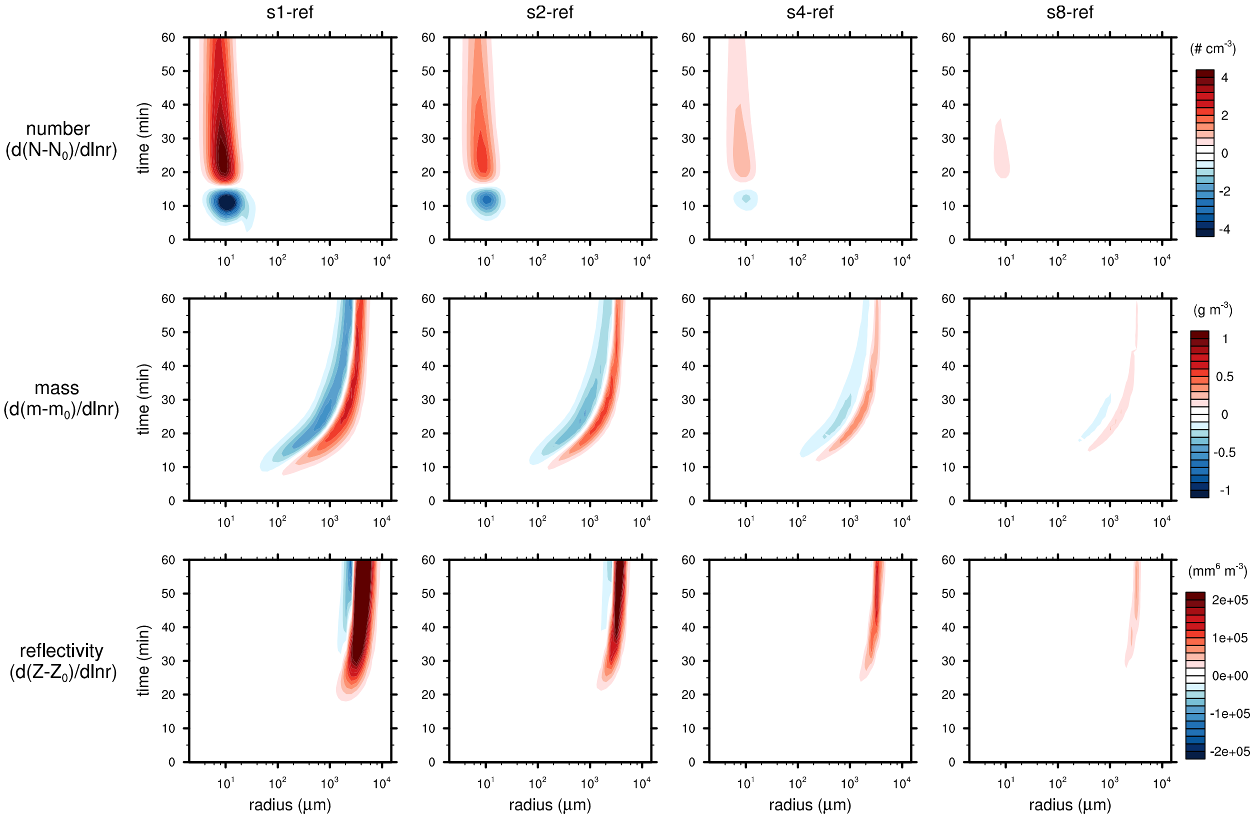

Fig. 2. Time evolutions of difference in size distributions of (top) number, (middle) mass, and (bottom) radar reflectivity factor of drops to the reference solution (s = 64) when (first column) s = 1, (second column) s = 2, (third column) s = 4, and (fourth column) s = 8 obtained using the J94 scheme. Δt = 1 s for all mass grids.

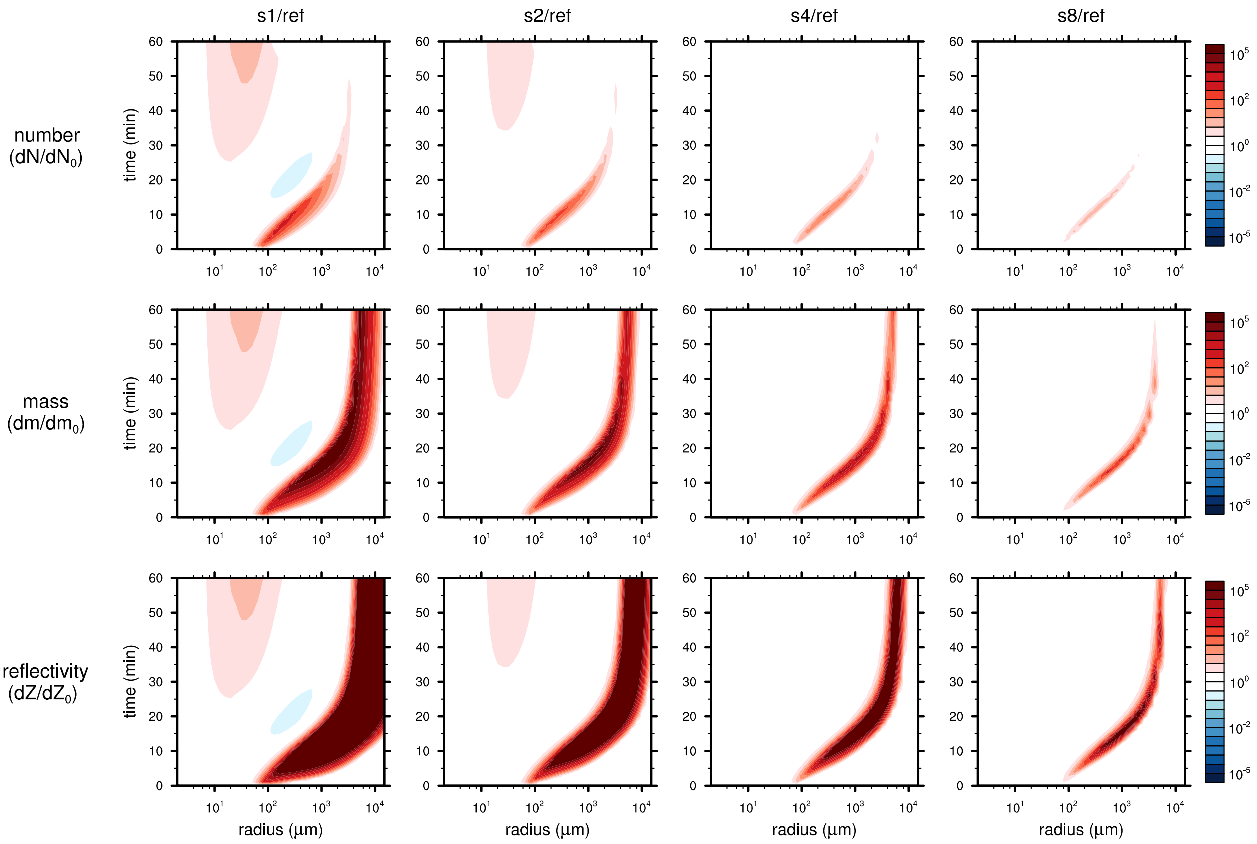

686

687 Fig. 3. As in Fig. 2, but for the ratio of the solutions to the reference solution.

688

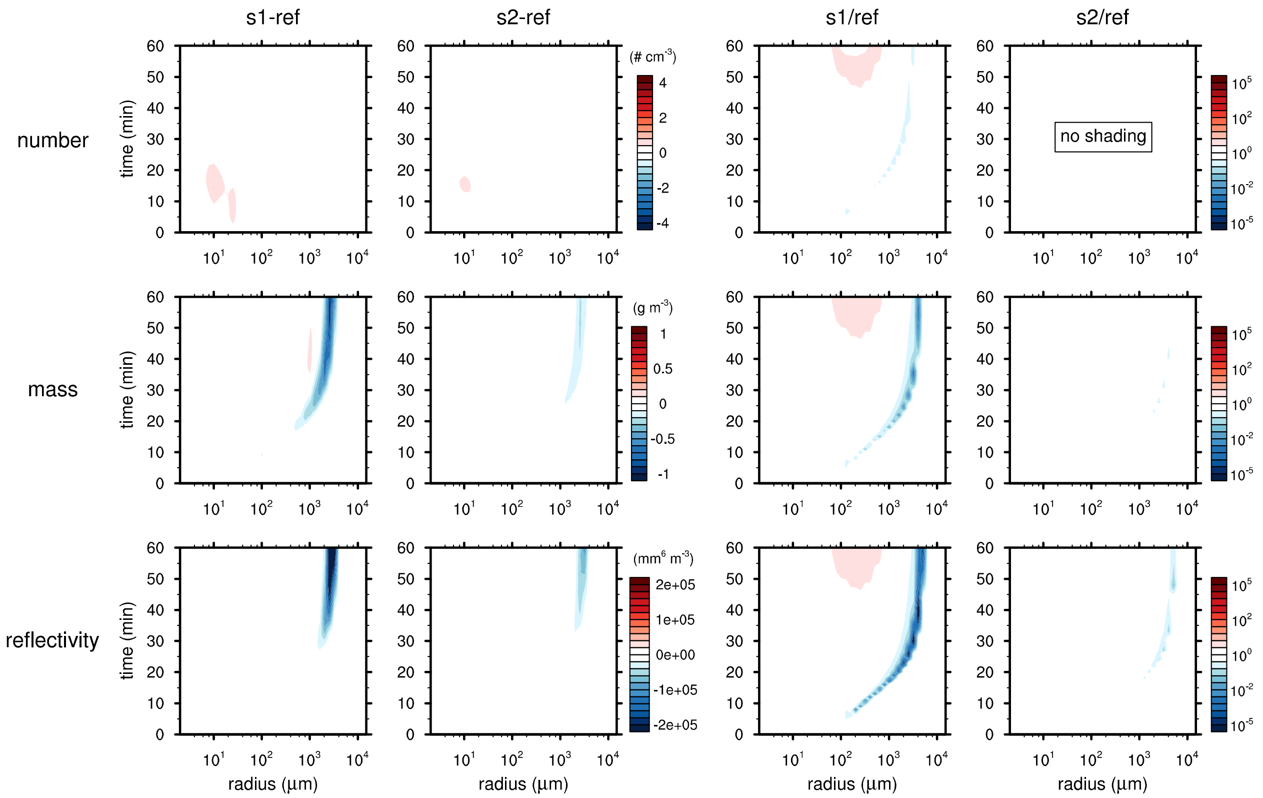

Fig. 4. Leftmost two columns as in Fig. 2, but obtained using the BR74 scheme when (first) $s = 1$ and (second) $s = 2$. Rightmost two columns as in Fig. 3, but obtained using the BR74 scheme when (third) $s = 1$ and (fourth) $s = 2$. $\Delta t = 0.1$ s for all mass grids. Note that there is no shading with the legend in the plot of ratio of the size distribution of drop number to the reference solution when $s = 2$.

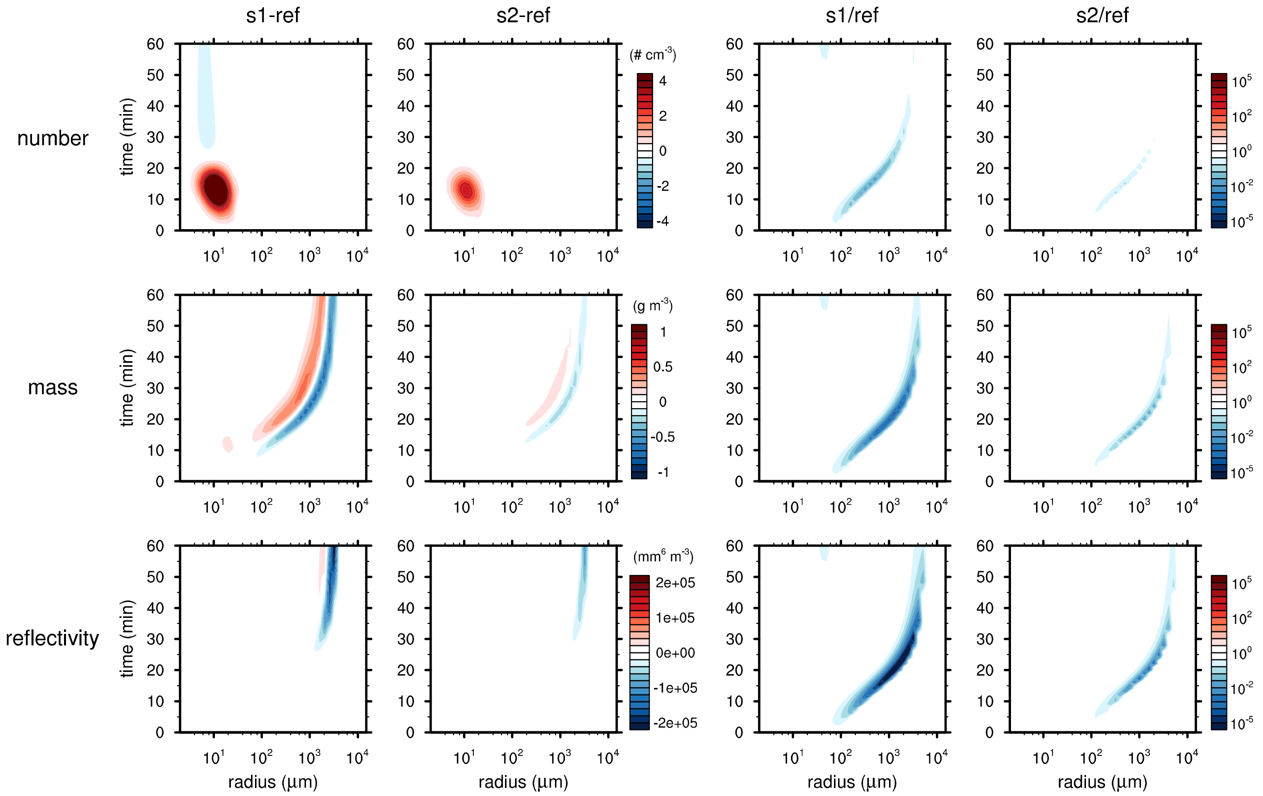

Fig. 5. As in Fig. 4, but obtained using the B00 scheme. Δ*t* = 1 s for all mass grids.

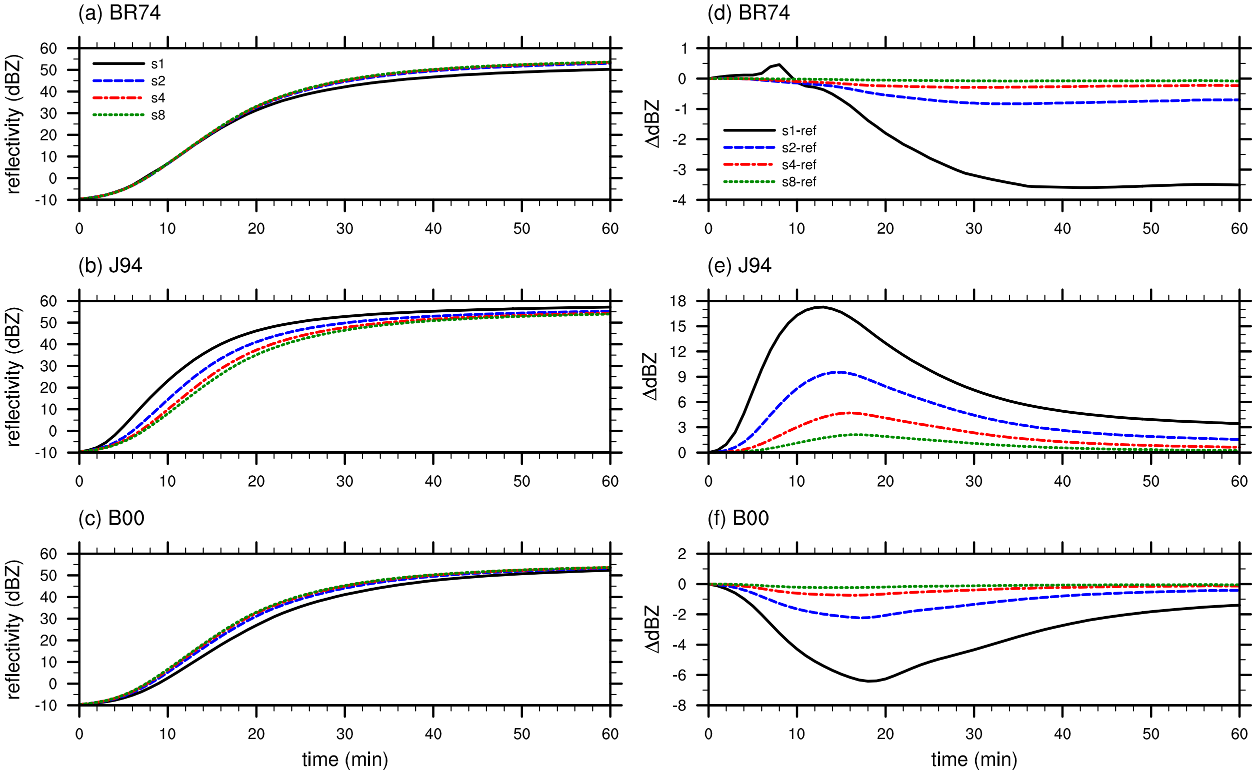

Fig. 6. Time series of total radar reflectivity factor obtained using (a) the BR74 scheme, (b) the J94 scheme, and (c) the B00 scheme with mass bin width parameter *s* varied from 1 to 8. Time step is 1 s for the J94 and B00 schemes and 0.1 s for the BR74 scheme. (d)–(f) are the same as (a)–(c) but for the deviations from the reference solution. Note that (d)–(f) use their own scales.

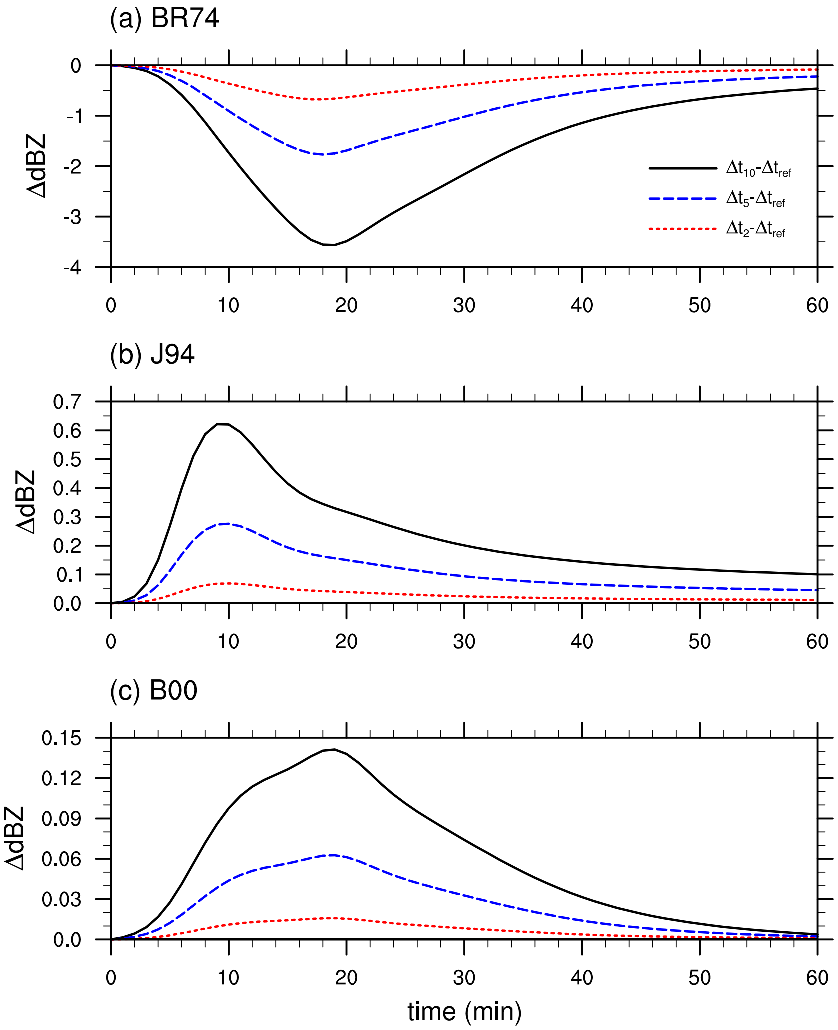

Fig. 7. Time series of deviations of total radar reflectivity factor from that with the fixed time step (0.1 s for the BR74 scheme and 1 s for the J94 and B00 schemes) obtained using (a) the BR74 scheme, (b) the J94 scheme, and (c) the B00 scheme with varied time steps from 10 s to 2 s. The parameter *s* is set to 2. Note that each plot uses its own scale.

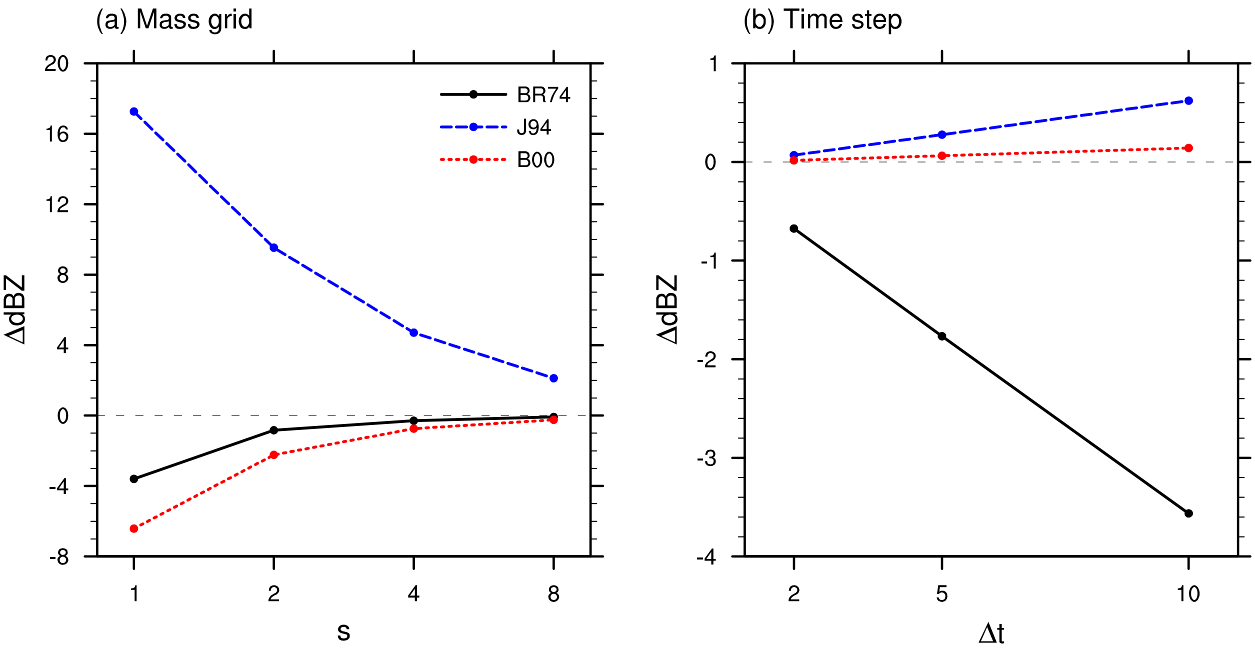

Fig. 8. The maximum deviations in the total radar reflectivity factor as a function of (a) the bin width parameter *s* and (b) model time step. In (a), the model time step is fixed at 1 s for the J94 and the B00 schemes and 0.1 s for the BR74 scheme. The reference solution (Fig. 1) is used to calculate the deviations. In (b), the bin width parameter *s* is fixed at 2. The solutions obtained using $s = 2$ and $\Delta t = 1$ s (J94 and B00) and 0.1 s (BR74) are used to calculate the deviations, respectively.

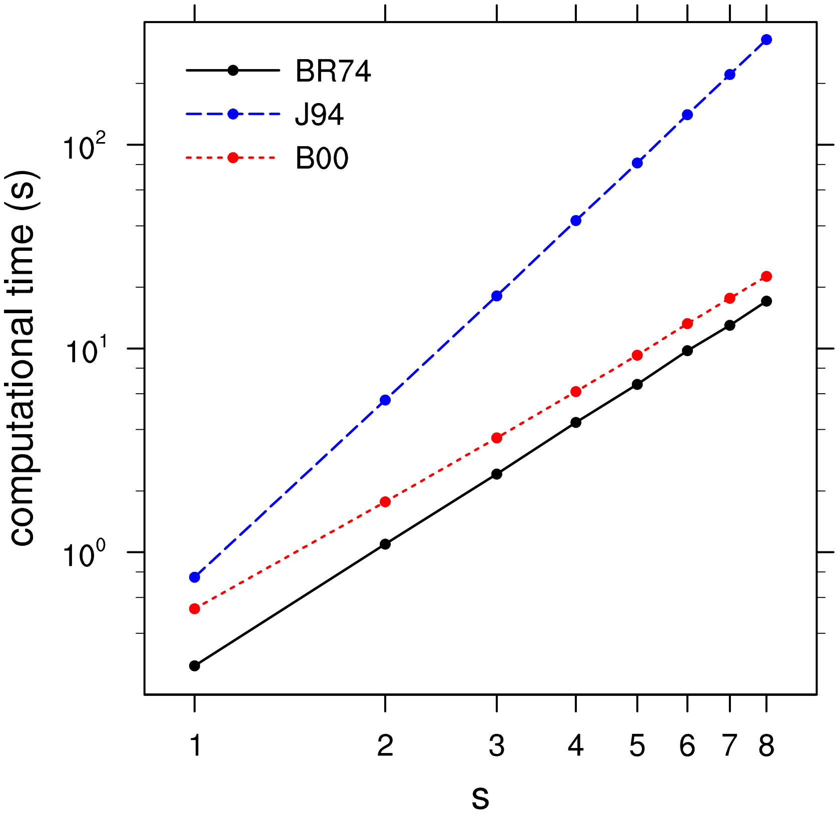

Fig. 9. Computational time required for 1-h integration of the box model using the BR74, J94, and B00 schemes with bin width parameter *s* varied from 1 to 8. Time step is 1 s.

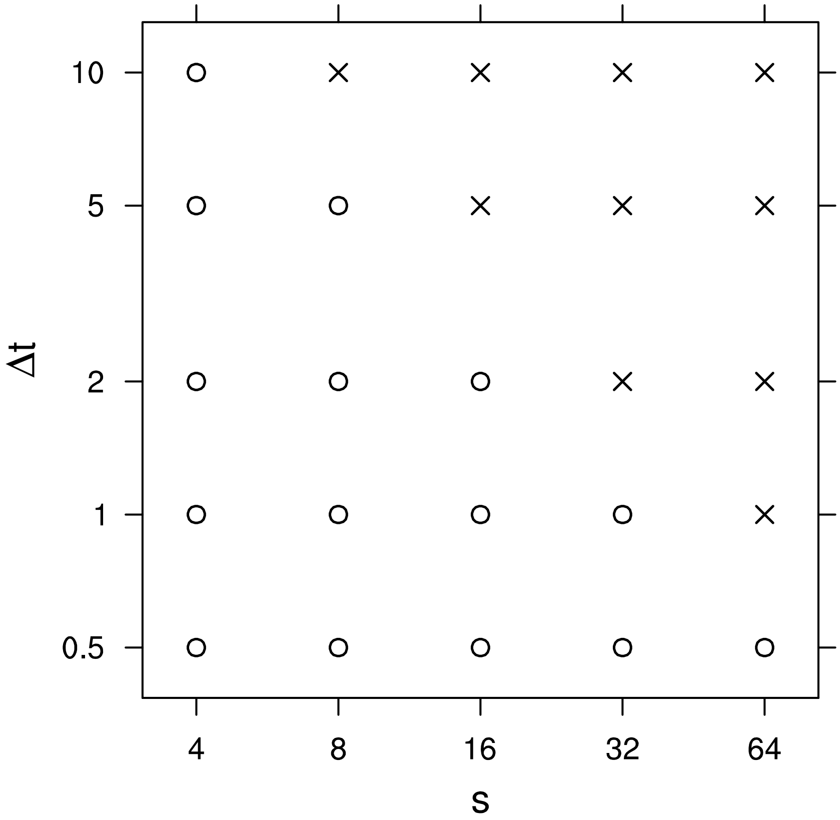

Fig. 10. Numerical stability of the BR74 scheme with varied bin width parameter *s* and time step. A circle indicates the scheme is stable and an X indicates the scheme is unstable.

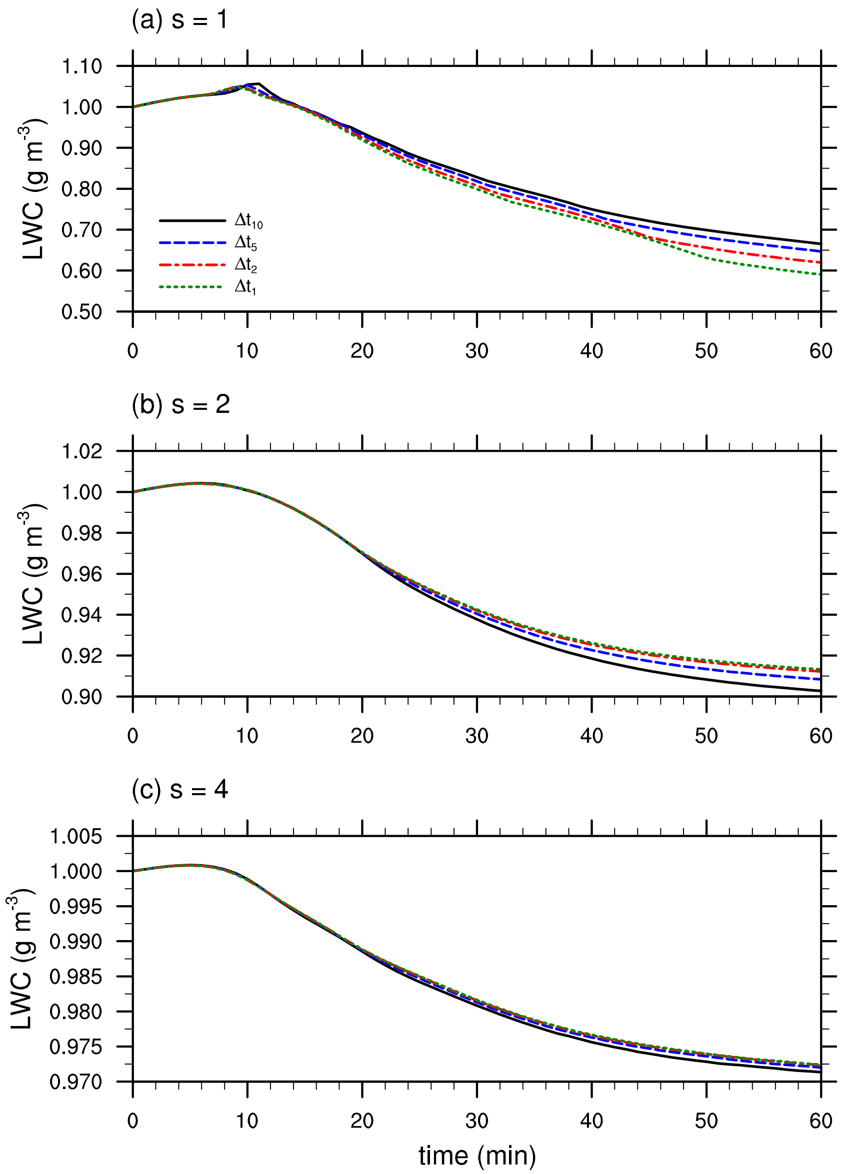

Fig. 11. Time series of the total drop mass when *s* = (a) 1, (b) 2, and (c) 4 using the BR74 scheme. Time step is varied from 10 to 1 s.

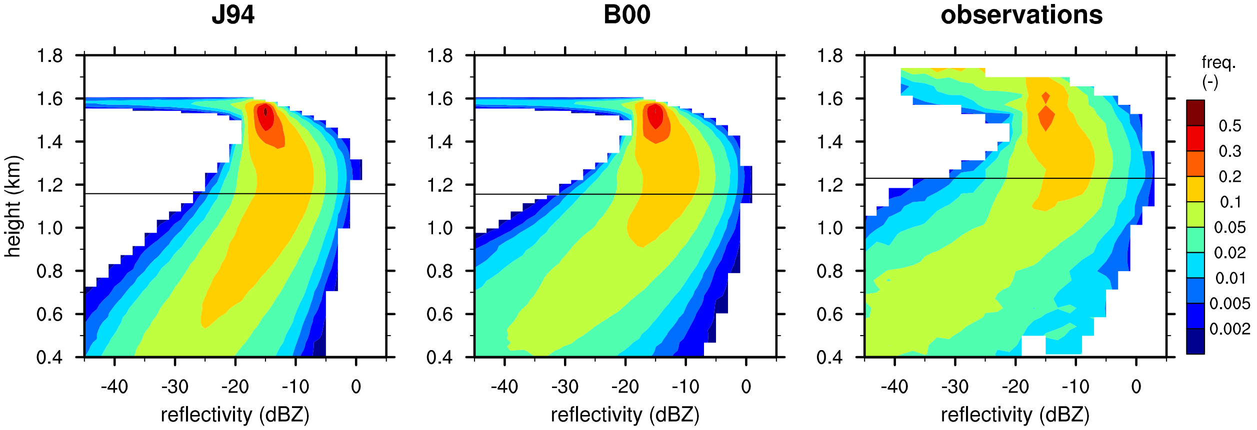

Fig. 12. Contoured frequency by altitude diagrams of radar reflectivity factor obtained using (left) the J94, (center) the B00 scheme, and (right) from observations. Black lines indicate the mean cloud base heights, in which cloud base is defined as the lowest grid cell where visible extinction exceeds 1 km^{-1}, as in Rémillard et al. (2017).

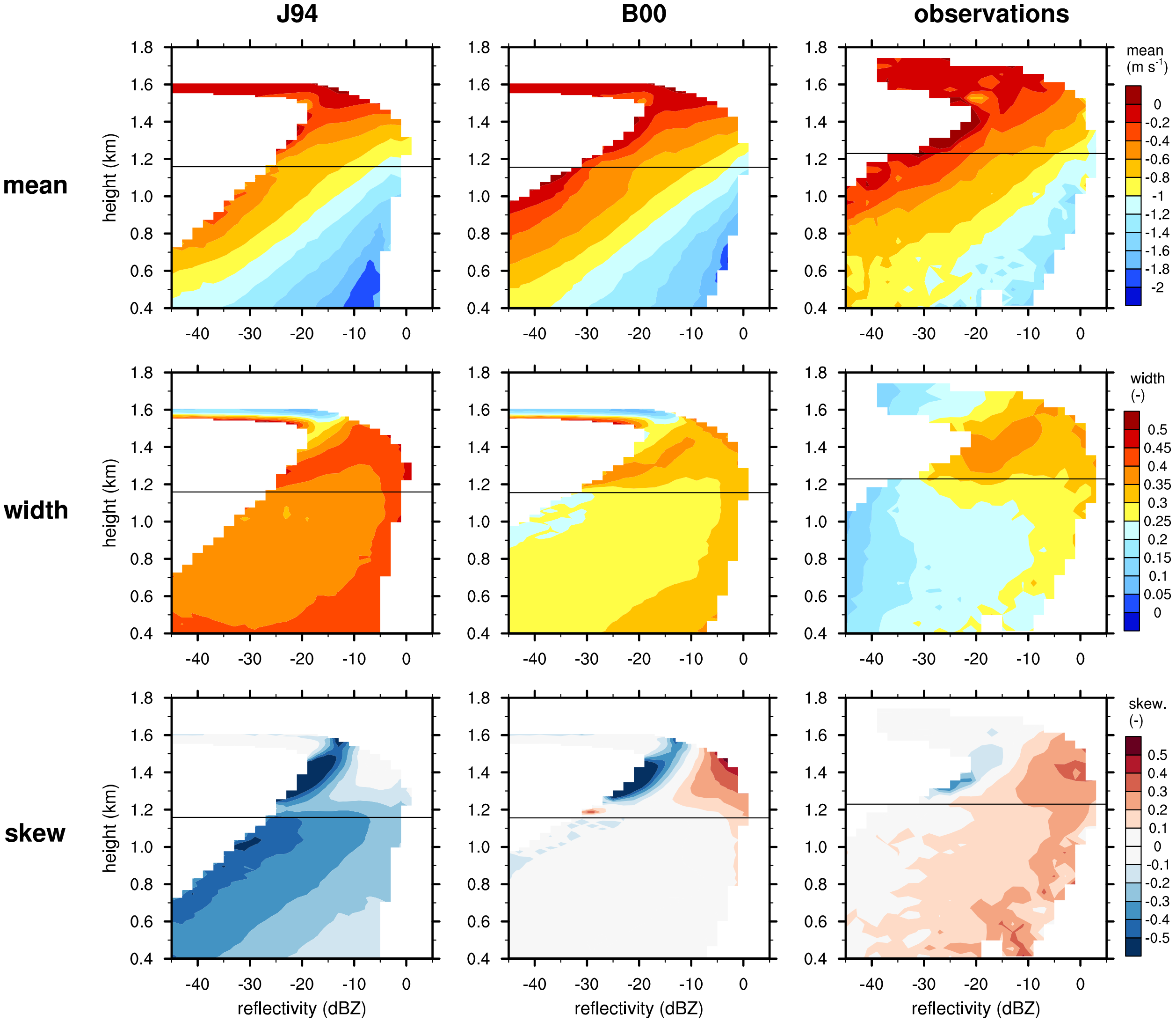

Fig. 13. Median of (top) mean Doppler velocity, (middle) width of Doppler spectra, and (bottom) skewness of Doppler spectra for a given radar reflectivity factor range and height obtained using (left) the J94, (center) the B00 scheme, and (right) from observations. The sign convention for Doppler velocities is negative for downward motion. Black lines indicate the mean cloud base heights.

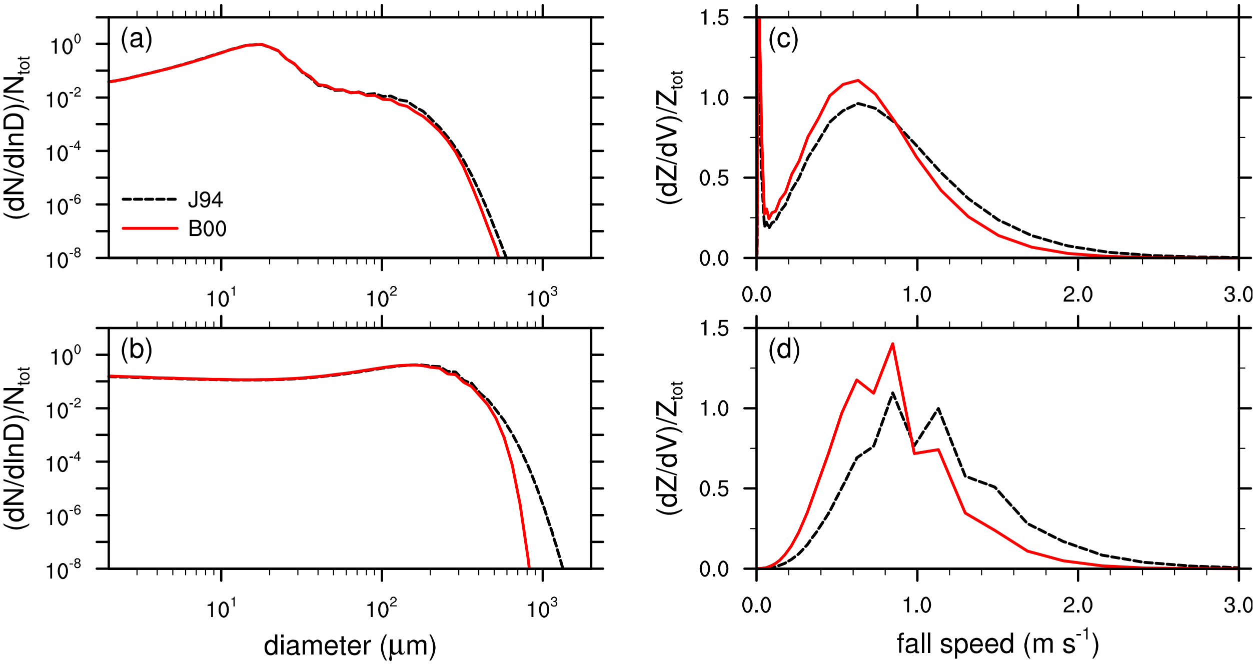

Fig. 14. Normalized size distributions of drop number concentration at *z* = (a) 1.2 km (which is close to mean cloud base) and (b) 1.0 km obtained using the J94 and B00 schemes. (c) and (d) are the same as (a) and (b) but for radar reflectivity factors as a function of drop fall speed. Normalization is by total drop number concentration in (a) and (b) and by total radar reflectivity factor in (c) and (d).